Image resolution and image contrast in the electron microscope. III. Inelastic scattering and coherent illumination

1973 J. Phys. A: Math. Nucl. Gen. 6 218

(http://iopscience.iop.org/0301-0015/6/2/012)

J. Phys. A: Math., Nucl. Gen., Vol. 6, February 1973. Printed in Great Britain.

Image resolution and image contrast in the electron microscope III. Inelastic scattering and coherent illumination

D L Misell and A J Atkins

Department of Physics, Queen Elizabeth College, Campden Hill Road, London, W8 7AH, UK

MS received 8 August 1972

Abstract. The present work evaluates the effect of lens aberrations on image resolution and image contrast in the transmission electron microscope for the inelastic component of the electron beam; coherent illumination is assumed. An evaluation is made of the effect of chromatic aberration on the image resolution for inelastic scattering from an amorphous specimen in the 10–100 nm thickness range. It is found that, for a specimen characterized by a carbon-like electron energy loss spectrum, the adverse effect of chromatic aberration may be minimized by underfocus of the objective lens. The effect of the objective aperture size on the image resolution is examined for semi-angles in the range 0·005–0·015 rad. The effect of spherical aberration, in comparison with chromatic aberration, is not significant for small defocus values (0 to −200 nm) but spherical aberration has an effect on image resolution for defocus values of about −500 nm for an objective aperture of 0·015 rad. It is shown that the coherence energy interval of the inelastic scattering has little effect on image resolution. A comparison is made for a specimen thickness of 10 nm of the inelastic image and the dark- and bright-field elastic images. It is found that, although the ratio of elastic to inelastic scattering within the objective aperture is significantly less than unity, the elastic dark-field and inelastic image intensities are comparable. In bright-field microscopy phase contrast effects for the elastic component are important and the contribution of the inelastic image to the total image intensity is only as a slowly varying background. In the bright-field microscopy of thin specimens the main consideration is optimizing the elastic image contrast and resolution.

1. Introduction

In the electron microscopy of biological materials the adverse effect of chromatic aberration on the inelastic image resolution is well known (eg Cosslett 1969) but a comparison of the inelastic and elastic images using a wave-optical formulation is required in order to assess the effect of inelastic scattering on the total image intensity. The analysis of Kanaya *et al* (Kanaya *et al* 1954, Kanaya 1956a, b, 1957) is orientated towards crystalline specimens and no quantitative evaluation is made on the loss in image resolution as a result of chromatic aberration. Further, Kanaya seems to have used only a single energy loss value instead of the complete distribution of energy loss; single scattering conditions are assumed. The present work attempts to evaluate the effect of chromatic aberration on image resolution for an incident electron energy of 100 keV and for a series of amorphous specimens in the thickness range $t = 10$–100 nm. The predominance of inelastic electron scattering in unstained biological and polymeric materials for objective aperture sizes, semi-angle α subtended at the specimen, in the range 0·005–0·015 rad is clearly shown by the inelastic/elastic ratio I/E for $t = 10$ nm:

$\alpha = 0{\cdot}005$ rad, $I/E = 17$; $\alpha = 0{\cdot}01$ rad, $I/E = 6$; $\alpha = 0{\cdot}015$ rad, $I/E = 4$ (for carbon). In the conventional transmission electron microscope the inelastic image is severely affected by chromatic aberration and the image contrast is reduced by the essential chromatic incoherence of inelastic scattering. In the scanning transmission electron microscope the chromatic aberration constant is effectively zero, and the only chromatic aberration effect is due to the incident beam energy spread (less than 0·2 eV). The present calculations of the inelastic image, using the model given in § 2, are orientated towards the conventional microscope; the optimum resolution attainable in the inelastic image is examined in § 3. We show in § 4 the small effect of spherical aberration and partial chromatic coherence on the inelastic image resolution. A comparison is made in §§ 5 and 6 of the inelastic image intensity with the dark- and bright-field elastic images for $t = 10$ nm; in addition the corresponding inelastic images obtained in the scanning transmission electron microscope are given. In all calculations coherent illumination of the specimen is assumed.

2. The model for inelastic electron scattering

The equation for the inelastic image intensity $j_i(\boldsymbol{r}_i)$ in the image plane is, for unit magnification $M = 1$ (Misell 1971b),

$$j_i(\boldsymbol{r}_i) = \sum_{n=1}^{\infty} \int_0^{\infty} \left(\frac{K}{2\pi}\right)^2 \left| \int \Phi_n(E, \boldsymbol{\theta}) H(E, \boldsymbol{\theta}) \exp(-\mathrm{i}K\boldsymbol{\theta} \cdot \boldsymbol{r}_i)\, \mathrm{d}\boldsymbol{\theta} \right|^2 \mathrm{d}E \tag{1}$$

for the incoherent superposition of the n times inelastically scattered electron, defined by the wavefunction $\Phi_n(E, \boldsymbol{\theta})$ for an angle of scattering $\boldsymbol{\theta}$ and energy loss E. The term $K = 2\pi/\lambda$ and the wavelength λ of the scattered electron is dependent on E. The function $H(E, \boldsymbol{\theta})$ is the wave aberration function including spherical aberration (coefficient C_s), chromatic aberration (coefficient C_c) and defocusing (Δf) (eg Kanaya 1956b, Misell 1971b):

with

$$\left.\begin{aligned} H(E, \boldsymbol{\theta}) &= \exp(-\mathrm{i}K\gamma(E, \boldsymbol{\theta}))D(\boldsymbol{\theta}) \\ \gamma(E, \boldsymbol{\theta}) &= \frac{C_s\theta^4}{4} + \frac{C_c E\theta^2}{2E_0} + \frac{\Delta f\theta^2}{2} \end{aligned}\right\} \tag{2}$$

for an incident electron energy E_0; $D(\boldsymbol{\theta})$ is the aperture function defined as unity for the transparent parts of the objective aperture and zero for the opaque parts. In the present work C_s and C_c values of 2 mm, corresponding to the values in commercially available instruments, are used and $\Delta f < 0$ corresponds to underfocus of the objective lens.

In the calculations of the wavefunctions $\Phi_n(E, \boldsymbol{\theta})$ we have made three assumptions.

(i) The spatial coherence of the inelastic wave. Because of the small-angle nature of inelastic electron scattering it can be shown that, for plasmon excitation, the inelastic wave is coherent over all $\boldsymbol{\theta}$ (Howie 1963). The spatial coherence of the inelastic scattering at large angles is doubtful, particularly if we include the effects of plural inelastic scattering. We rewrite the wavefunction $\Phi_n(E, \boldsymbol{\theta})$ in terms of phase factors as $\Phi_n(E, \boldsymbol{\theta}) = |\Phi_n(E, \boldsymbol{\theta})| \exp(\mathrm{i}\mu_n(\boldsymbol{\theta})) \exp(\mathrm{i}\sigma_n(E))$; the assumption of spatial coherence corresponds to $\mu_n(\boldsymbol{\theta}) = \mu_n$ independent of $\boldsymbol{\theta}$. Since Φ_n occurs in equation (1) as $\Phi_n(E, \boldsymbol{\theta})\Phi_n^*(E, \boldsymbol{\theta}')$ the μ_n terms cancel as well as the $\sigma_n(E)$ terms, as a result of the incoherent

superposition of electrons with different E. The problem of evaluating the $\Phi_n(E, \theta)$ reduces, under the assumption of spatial coherence, to a calculation of $|\Phi_n(E, \theta)|$ or experimentally we can determine $|\Phi_n|^2$.

(ii) The localization of inelastic scattering. It is assumed that, for inelastic electron scattering in amorphous biological specimens, the inelastic scattering is a localized phenomenon and Φ_n is characteristic of the specimen structure on a short range scale (Misell 1971b).

(iii) The separation of the energy and angular dependent terms. We neglect the dispersion relationship between E and θ and assume that all electrons with a given n are characterized by the angular distribution $|\phi_n(\theta)|^2$ irrespective of E (see below).

Assumptions (i) and (ii) favour the inelastic scattering in respect of forming a well defined image. In the case of crystalline specimens, where the energy loss distribution may be of a discrete nature, the delocalization for plasmon excitation is about 2 nm, which is at least comparable with the chromatic defect of the inelastic image.

The $|\Phi_n(E, \theta)|$ are calculated using

$$|\Phi_n(E, \theta)|^2 = P_n D_n(E, \theta) \simeq P_n Q_n(\theta) f_n(E), \tag{3}$$

where P_n is the Poisson distribution $(t/\Lambda_I)^n \exp(-t/\Lambda_I)/n!$ for n independent scattering processes each characterized by a mean free path Λ_I. $Q_n(\theta) = |\phi_n(\theta)|^2$ is the angular distribution after n inelastic interactions with energy distribution $f_n(E)$. For amorphous specimens the $Q_n(\theta)$ are calculated using a composite plasmon excitation/free atom/one electron excitation model (eg Doyle 1970), although the precise scattering model does not significantly affect the inelastic image results given in § 3. In the absence of experimental data on the angular–energy distributions D_n we make the approximation that D_n is a separable function of θ and E. In the calculation of inelastic scattering by single crystals this problem has been avoided by assuming a discrete energy loss, $\delta(E - E_p)$ (Doyle 1971).

Calculations have been made for $D_n(E, \theta)$ characteristic of electron scattering from 10, 50 and 100 nm of amorphous carbon for an incident electron energy of $E_0 = 100$ keV. Results for the total inelastic intensity

$$D(E, \theta) = \sum_{n=1}^{\infty} |\Phi_n(E, \theta)|^2 \tag{4}$$

are presented in figure 1 for $t = 10$ nm (figure 1(a)), $t = 50$ nm (figure 1(*b*)) and $t = 100$ nm (figure 1(c)) for $E_0 = 100$ keV ($\Lambda_I = 77{\cdot}5$ nm, $\Lambda_E = 131{\cdot}4$ nm); the values for the angle of scattering θ are 0·005 rad (full curve), 0·01 rad (broken curve) and 0·015 rad (chain curve) corresponding to the range of α values examined. As the thickness t increases the contributions from plural scattering, which give rise to the peak near 50 eV ($\sim 2 \times 25$ eV), increase. Because of the larger scattering angles for plural scattering, the contribution from this 50 eV peak, relative to the 25 eV maximum, generally increases with θ. This behaviour is clearly seen if we compare the results for $\theta = 0{\cdot}001$ rad and $\theta = 0{\cdot}005$ rad (figure 2) for $t = 10$ nm (figure 2(*a*)), $t = 50$ nm (figure 2(*b*)) and $t = 100$ nm (figure 2(*c*)). The essential small-angle behaviour of the inelastic scattering is shown by the large factor between the $D(E, \theta)$ curves for these two angles of scattering. (Note that the factor $2\pi\theta$ is used in figures 1 and 2 to reduce the $D(E, \theta)$ curves to a single scale.) An important feature of the $D(E, \theta)$ curves shown in figures 1 and 2 is the relatively small contribution from the 50 eV peak, and for the specimen thickness range 10–100 nm we do not expect

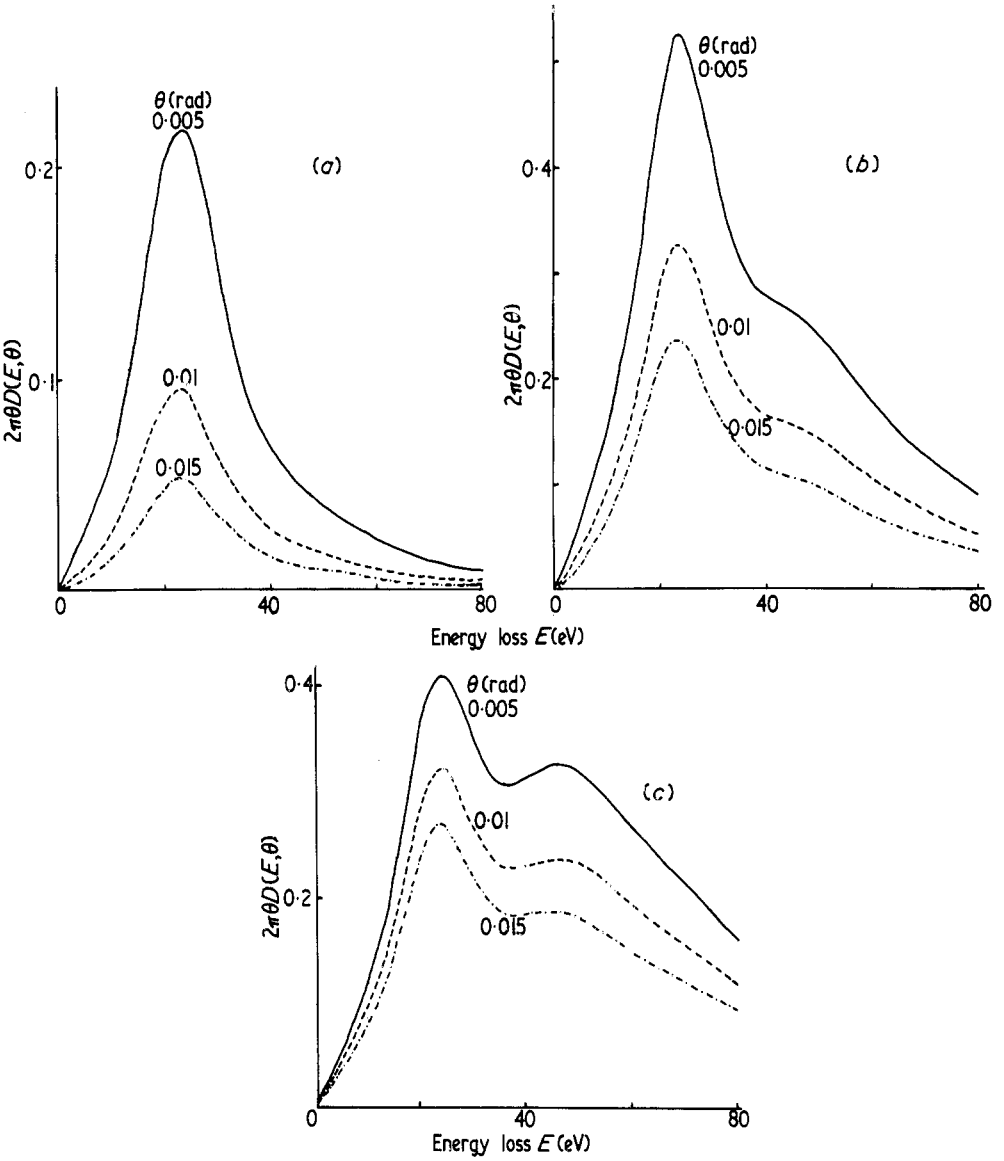

Figure 1. The variation of the electron energy loss spectrum of carbon $D(E, \theta)$ with the angle of scattering θ. The incident electron energy is 100 keV and the specimen thickness is (*a*) 10 nm, (*b*) 50 nm, (*c*) 100 nm.

the chromatic aberration, arising as a result of the energy loss distribution, to vary significantly with film thickness. It is not until t exceeds 200 nm that the loss at 50 eV is dominant for these small angles of scattering.

3. Calculation of the inelastic image

We consider in this section the numerical results for the inelastic image intensity calculated for scattering from 10–100 nm of amorphous carbon with $E_0 = 100$ keV; film

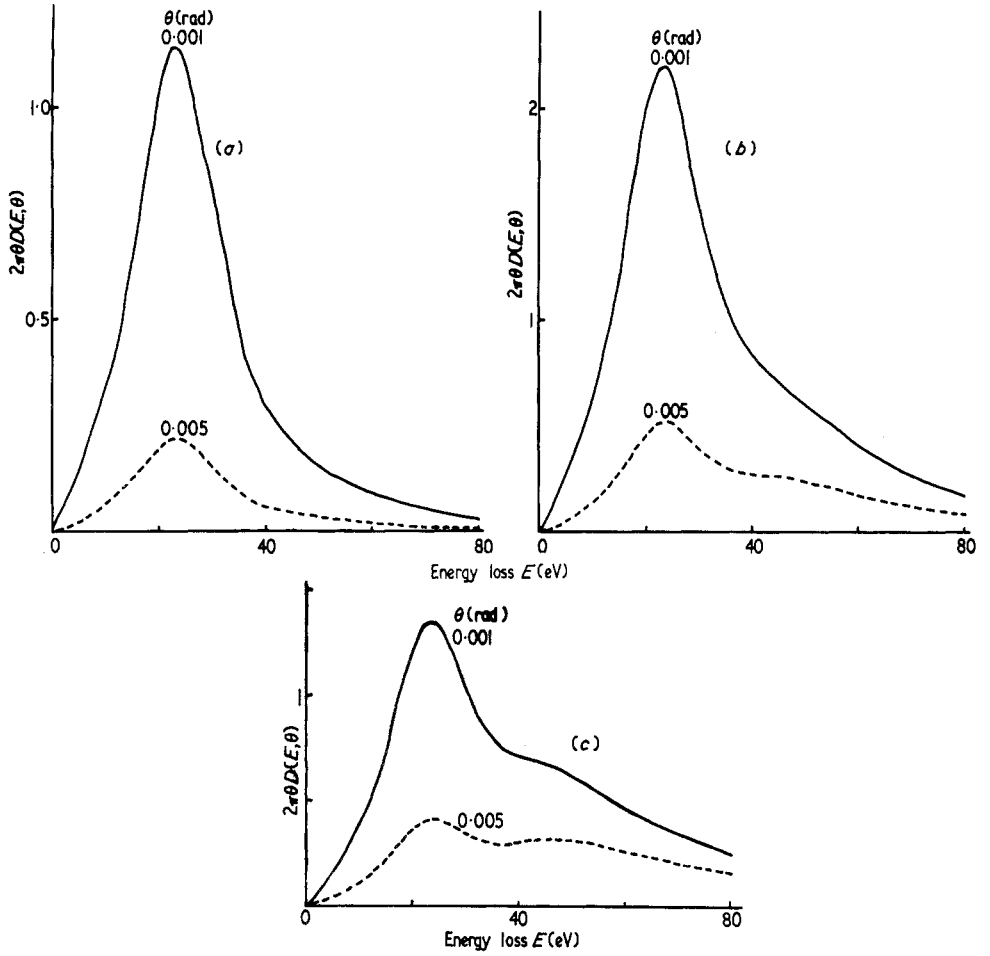

Figure 2. The variation of the electron energy loss spectrum of carbon $D(E, \theta)$ with the angle of scattering θ. The incident electron energy is 100 keV and the specimen thickness is (*a*) 10 nm, (*b*) 50 nm, (*c*) 100 nm.

thickness above 100 nm are of little interest to the microscopist and a section of a biological material is usually in the 10–50 nm thickness range. In figure 3 are shown the radial profiles for the inelastic image intensity $j_i(r_i)$ for $t = 10$ nm and two objective aperture values: $\alpha = 0{\cdot}005$ rad (figure 3(*a*)) and 0·01 rad (figure 3(*b*)), including both the effects of chromatic and spherical aberration (aberration constants $C_s = C_c = 2$ mm), and for a series of defocus values Δf. It is seen that the $\Delta f = 0$ curve, which corresponds to focusing on $E \simeq 0$, has a large radial halfwidth (about 1·8 nm) but that underfocus values near -500 nm give a maximum in $j_i(0)$ and a significantly reduced radial halfwidth of the image profile (about 0·5 nm). This is in agreement with the results of Kanaya (1956a,b) who predicts an optimum Δf for the inelastic image based on the most probable energy loss E_{mp} ($\simeq 25$ eV for carbon):

$$\Delta f_i \simeq -C_c E_{mp}/E_0$$

corresponding to the partial cancellation of the chromatic aberration by underfocus

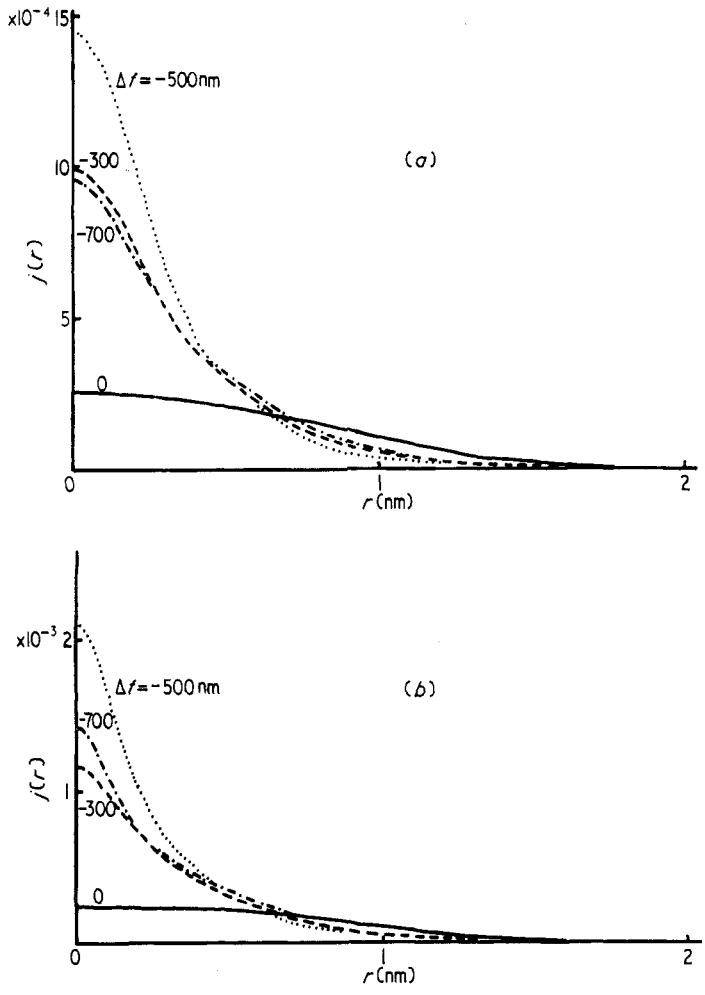

Figure 3. The inelastic image intensity $j(r)$ and its variation with defocus Δf for an objective aperture of semi-angle α: (*a*) 0·005 rad, (*b*) 0·01 rad for a specimen thickness $t = 10$ nm. $C_s = C_c = 2$ mm, $E_0 = 100$ keV.

of the objective lens. Although the radial halfwidth $r_{1/2}$ of the inelastic image profile $j_i(\boldsymbol{r}_i)$ is a useful guide to the chromatic aberration defect, this quantity does not indicate the loss in resolution arising from the large r_i behaviour of j_i. The integral $\int j_i(\boldsymbol{r}_i)\,\mathrm{d}\boldsymbol{r}_i$, representing the total inelastic scattering within the objective aperture α, $h_I(\alpha)$, converges to h_I for radial distances $r_i \simeq 4$ nm with $t = 10$ nm. The small-angle behaviour of the inelastic scattering is shown by the small differences between the corresponding inelastic images for $\alpha = 0{\cdot}01$ rad and $\alpha = 0{\cdot}015$ rad (figure 4). For the larger defocus values, $\Delta f \simeq -700$ nm (figure 4(*b*)), the radial halfwidth of j_i is significantly less for the larger aperture, although the two sets of curves coincide for $r_i > 0{\cdot}5$ nm. This reduction in $r_{1/2}$ at the larger defocus values is attributed to the more effective cancellation of the increased spherical aberration for the larger aperture, and a reduction in the diffraction limit (evident only when $r_{1/2}$ is less than 0·5 nm). On the latter point we remark that although the inelastic angular distribution decreases as $(\theta^2 + \theta_E^2)^{-1}$, the wavefunction

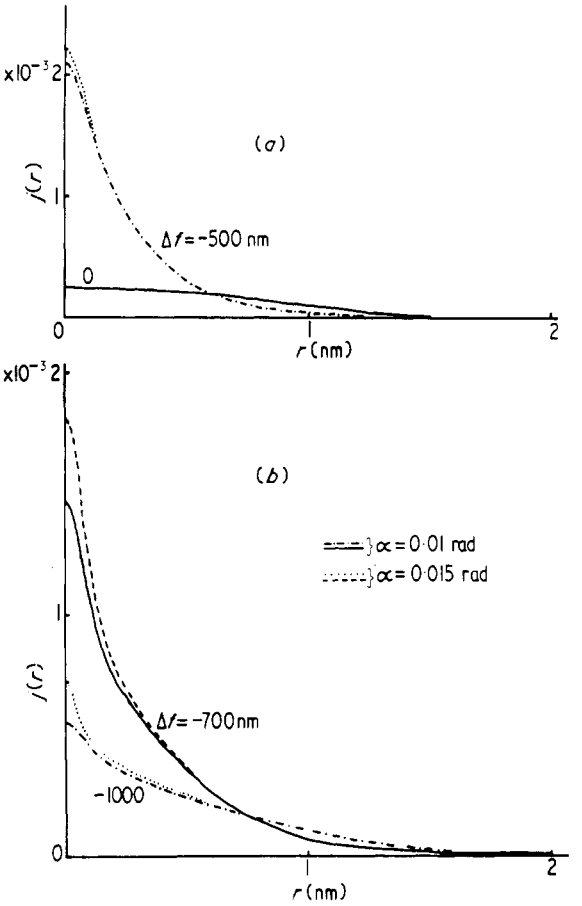

Figure 4. A comparison of the inelastic image intensity $j(r)$ for $\alpha = 0{\cdot}01$ rad and $\alpha = 0{\cdot}015$ rad for a series of defocus values Δf: (*a*) 0 and -500 nm, (*b*) -700 and -1000 nm and a specimen thickness $t = 10$ nm. $C_s = C_c = 2$ mm, $E_0 = 100$ keV.

decreases only as $|\phi_1(\boldsymbol{\theta})| \sim (\theta^2 + \theta_E^2)^{-1/2}$ in the inelastic image integral (equation (1)). The diffraction effect of the objective aperture on the inelastic image can be demonstrated by calculating j_i with $C_s = C_c = \Delta f = 0$ giving for $r_{1/2}$: $\alpha = 0{\cdot}01$ rad, $r_{1/2} = 0{\cdot}24$ nm; $\alpha = 0{\cdot}015$ rad, $r_{1/2} = 0{\cdot}16$ nm; thus this diffraction effect will only be evident when $r_{1/2}$ is small.

On the basis of the figures for $r_{1/2}$ it would appear that the inelastic image can, even in the presence of chromatic aberration, give high resolution images, but the slow convergence of j_i to zero at large radial distances leads to an overall inferior image resolution to that obtained in dark-field elastic images (see § 5). The optimum defocus Δf_I giving the maximum value in $j_i(0)$ varies from -480 to -570 nm for $\alpha = 0{\cdot}005$–$0{\cdot}015$ rad and $t = 10$ nm. With the above reservations on the meaning of $r_{1/2}$, we present in figure 5 the variation of $r_{1/2}$ with defocus Δf. We note that $r_{1/2}$ does not vary significantly with α, and the lowest values for $r_{1/2} = 0{\cdot}4$–$0{\cdot}5$ nm are a factor 2–4 lower than the estimates given by Cosslett (1969).

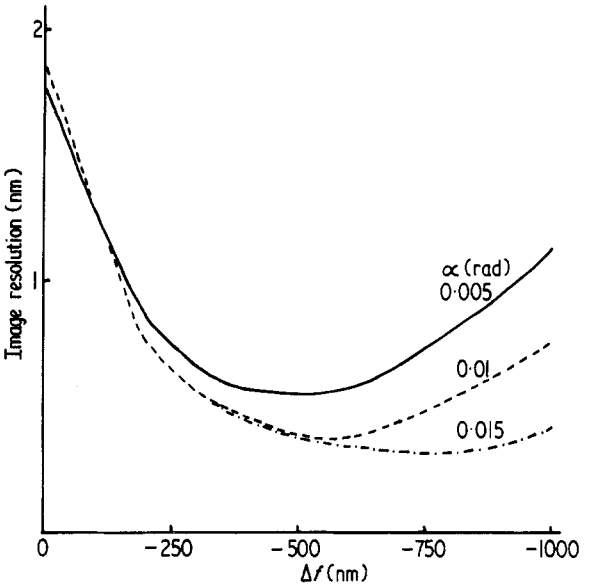

Figure 5. The inelastic image resolution, based on the radial halfwidth of $j(r)$, for $\alpha = 0{\cdot}005$, 0·01 and 0·015 rad and for a series of defocus values Δf with $t = 10$ nm. $C_s = C_c = 2$ mm, $E_0 = 100$ keV.

The behaviour of the inelastic image intensity for thicker films, $t = 50$ nm (compared with $t = 10$ nm in figure 6) and $t = 100$ nm (compared with $t = 50$ nm in figure 7) for $\alpha = 0{\cdot}015$ rad, shows clearly that $r_{1/2}$ varies only marginally with t. In figure 6 we compare j_i for $t = 10$ and 50 nm, where although $r_{1/2}$ increases by only 0·05 nm, we cannot infer that the image resolution does not deteriorate significantly with increasing t. The ratio h_{50}/h_{10} for scattering within the objective aperture is about 3 but the ratio of j_{50}/j_{10} is only 2 below 1 nm, increasing above 3 for larger radial distances. This behaviour is particularly marked for the $t = 50/100$ nm comparison (figure 7) where $h_{100}/h_{50} \simeq 1$ but j_{100}/j_{50} is significantly less than unity, although this ratio increases with larger underfocus values, corresponding to optimizing the image resolution by focusing near the secondary peak at 50 eV in the energy distribution for $t = 100$ nm. The optimum defocus Δf_i for maximum $j_i(0)$ increases from -570 to -620 nm for $t = 10$–100 nm and $\alpha = 0{\cdot}015$ rad. Figure 8 shows the variation of $r_{1/2}$ with the defocus Δf for the three specimen thicknesses 10, 50 and 100 nm. Again we emphasize that although $r_{1/2}$ increases only marginally with t, the radial convergence of j_i becomes slow; for $t = 50$ nm the integral of j_i over r_i converges to $h_i(\alpha)$ only for $r_i > 8$ nm.

4. The effect of spherical aberration and chromatic coherence on the inelastic image

4.1. The effect of spherical aberration

We compare the results for $j_i(r_i)$ in the absence of a spherical aberration term in equation (2) with the corresponding results for $C_s = 2$ mm (figure 9, $t = 10$ nm). For $\alpha = 0{\cdot}005$ rad the exclusion of spherical aberration has a negligible effect on the image intensity profile; the maximum value of the spherical aberration phase shift $KC_s\theta^4/4$ is only 0·55 rad

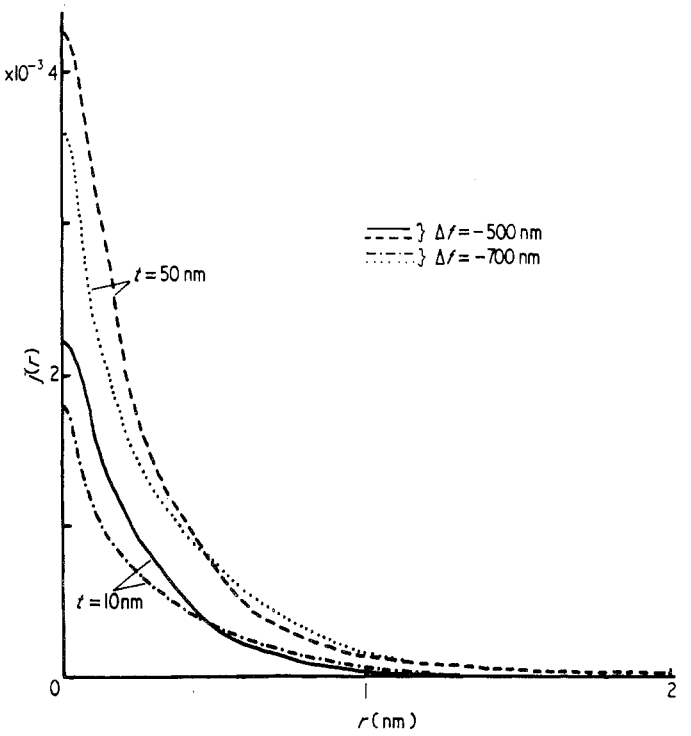

Figure 6. A comparison of the inelastic image intensity $j(r)$ for specimen thicknesses 10 and 50 nm for $\Delta f = -500, -700$ nm. $\alpha = 0{\cdot}015$ rad, $C_s = C_c = 2$ mm, $E_0 = 100$ keV.

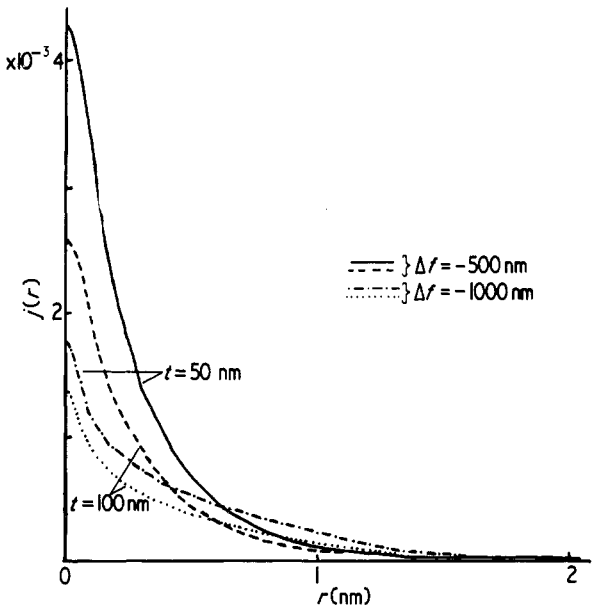

Figure 7. A comparison of the inelastic image intensity $j(r)$ for specimen thicknesses 50 and 100 nm for $\Delta f = -500, -1000$ nm. $\alpha = 0{\cdot}015$ rad, $C_s = C_c = 2$ mm, $E_0 = 100$ keV.

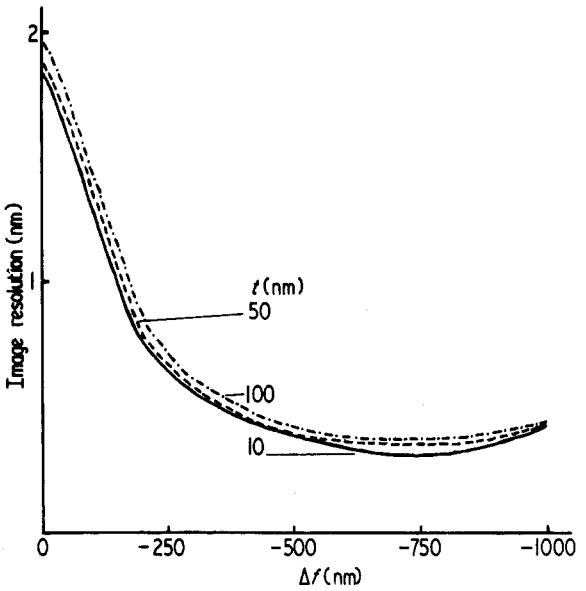

Figure 8. The inelastic image resolution, based on the radial halfwidth of $j(r)$ for t = 10, 50, 100 nm and for a series of defocus values Δf with α = 0·015 rad. $C_s = C_c$ = 2 mm, E_0 = 100 keV.

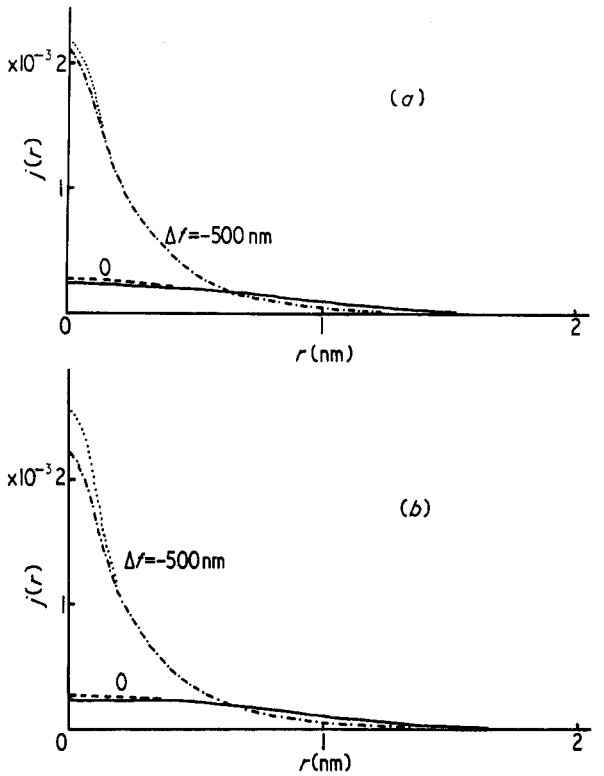

Figure 9. The effect of spherical aberration on the inelastic image intensity $j(r)$ for (*a*) α = 0·01 rad, (*b*) α = 0·015 rad for a specimen thickness t = 10 nm. C_c = 2 mm, E_0 = 100 keV. Full and chain curves, C_s = 2 mm; broken and dotted curves, C_s = 0.

corresponding to a small defocus -25 nm. However, at small radial distances the spherical aberration increases with α for 0·01 rad (figure 9(*a*)) and 0·015 rad (figure 9(*b*)), for example, for $\alpha = 0{\cdot}015$ rad $r_{1/2}$ increases from 1·82 to 1·84 nm for $\Delta f = 0$ and from 0·33 to 0·38 nm for $\Delta f = -500$ nm; as expected there is no effect on j_i at large radial distances.

4.2. *The effect of chromatic coherence*

In equation (1) we assume that inelastic electrons with different n and E are incoherent. Although it is unlikely that electrons with different n are coherent, it is possible that electrons with a given n are coherent within energy bands ΔE. In equation (1) we sum the contributions from electrons in a given ΔE centred on E coherently, but the contributions from electrons in different energy bands are superimposed incoherently (Misell 1971b). Figure 10 shows the dependence of j_i on ΔE for 1, 4 and 10 eV coherence intervals for $\Delta f = 0$. In both the case of $\alpha = 0{\cdot}005$ rad (figure 10(*a*)) and $\alpha = 0{\cdot}01$ rad (figure 10(*b*)) it is seen that the image profile improves only marginally with increasing

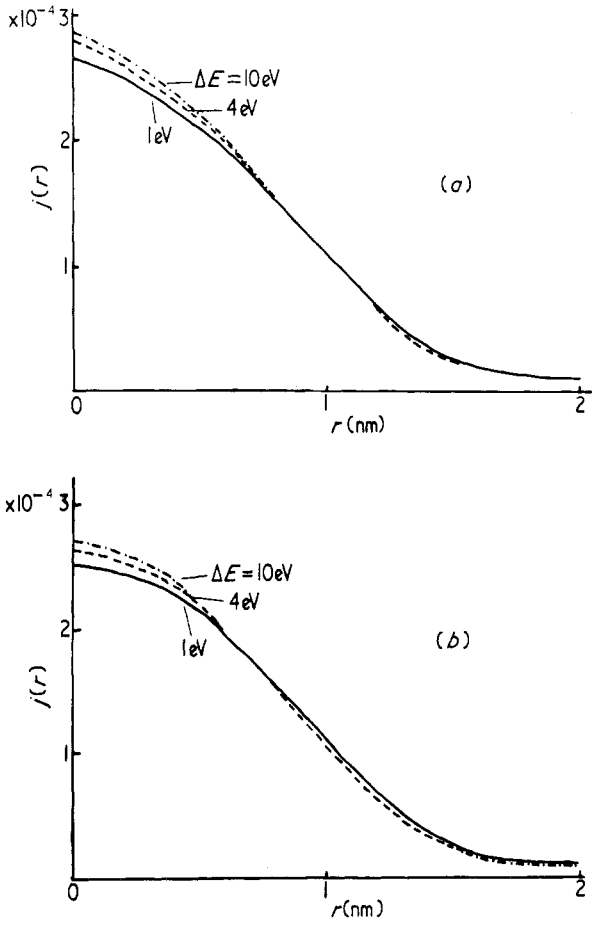

Figure 10. The effect of the chromatic coherence interval ΔE on the inelastic image intensity $j(r)$ for (*a*) $\alpha = 0{\cdot}005$ rad, (*b*) $\alpha = 0{\cdot}01$ rad for $t = 10$ nm. $C_s = C_c = 2$ mm, $E_0 = 100$ keV.

ΔE. As expected with increasing ΔE the value of $j_i(0)$ increases with a corresponding decrease in $r_{1/2}$. Any chromatic coherence imposed by using ΔE is destroyed by the chromatic aberration phase term in equation (2), $K(C_c E\theta^2/2E_0)$. Here the conventional electron microscope is unsuited to any judgement on chromatic coherence because of the dominance of chromatic aberration effects. The scanning transmission microscope, with no lens system after the specimen (Crewe 1970), is suited to such an evaluation.

5. Comparison of the inelastic image with the dark-field elastic image

In dark-field microscopy the unscattered component of the transmitted electron beam does not contribute to the image; thus phase contrast effects arising from the interference of the unscattered and elastic waves are absent in the dark-field elastic image. The elastic image wavefunction in dark-field is (eg Misell 1971a)

$$\psi_i(\boldsymbol{r}_i) = \frac{K_0}{2\pi} \int \Psi_E(\boldsymbol{\theta}) \exp(i\chi(\boldsymbol{\theta})) D(\boldsymbol{\theta}) \exp(-iK_0 \boldsymbol{\theta} \cdot \boldsymbol{r}_i)\, d\boldsymbol{\theta}. \tag{5}$$

$\Psi_E(\boldsymbol{\theta})$ is the elastically scattered wave, normalized such that

$$\int_0^{2\pi} \int_0^{\alpha} |\Psi_E(\boldsymbol{\theta})|^2 \, d\boldsymbol{\theta} = h_E(\alpha)$$

and Parseval's theorem relates the image intensity $j_i(\boldsymbol{r}_i) = |\psi_i(\boldsymbol{r}_i)|^2$ to $h_E(\alpha)$ by

$$\int |\psi_i(\boldsymbol{r}_i)|^2 \, d\boldsymbol{r}_i = h_E(\alpha).$$

$\chi(\boldsymbol{\theta})$ is the aberration function including only the spherical aberration and defocusing terms of equation (2).

In the present work we have calculated $\Psi_E(\boldsymbol{\theta})$ for scattering from a thin film ($t = 10$ nm) of amorphous carbon. Since the elastic mean free path $\Lambda_E \simeq 130$ nm ($E_0 = 100$ keV), $t/\Lambda_E \ll 1$ and single scattering conditions are valid for the elastic scattering. In the first Born approximation $\Psi_E(\boldsymbol{\theta})$ is calculated from

$$\Psi_E(\boldsymbol{\theta}) = \exp(i\pi/2) |\Psi_E(\boldsymbol{\theta})| \tag{6}$$

with

$$|\Psi_E(\boldsymbol{\theta})|^2 = (t/\Lambda_E) \exp(-t/\Lambda_T) R_1(\boldsymbol{\theta}).$$

$R_1(\boldsymbol{\theta})$ describes the angular distribution for elastic scattering by amorphous carbon. The elastic image intensity $j_i(\boldsymbol{r}_i)$ is shown in figure 11 for three α values (full curves) corresponding to the optimum defocus value Δf_E giving a maximum value for $j_i(0)$. The inelastic images corresponding respectively to Δf_E and Δf_I ($= -500$ nm) are shown in figure 11 as broken and chain curves. The final curve corresponds to the inelastic image that would be obtained in the scanning transmission microscope ($C_c = 0$, dotted curve). The rapid radial convergence to zero of the elastic image is reflected in the convergence of the integral of j_i over $\boldsymbol{r}_i$ to $h_E(\alpha)$ for $r_i \simeq 1$ nm. Except for the smallest aperture, 0·005 rad (figure 11(*a*)), the elastic image intensity is comparable with the best inelastic image ($C_c = 2$ mm), although significantly below the scanning microscope inelastic image ($C_c = 0$). Table 1 illustrates this behaviour by comparing the radial halfwidths $r_{1/2}$ and the ratio R of the inelastic image intensity to elastic image intensity at $r_i = 0$.

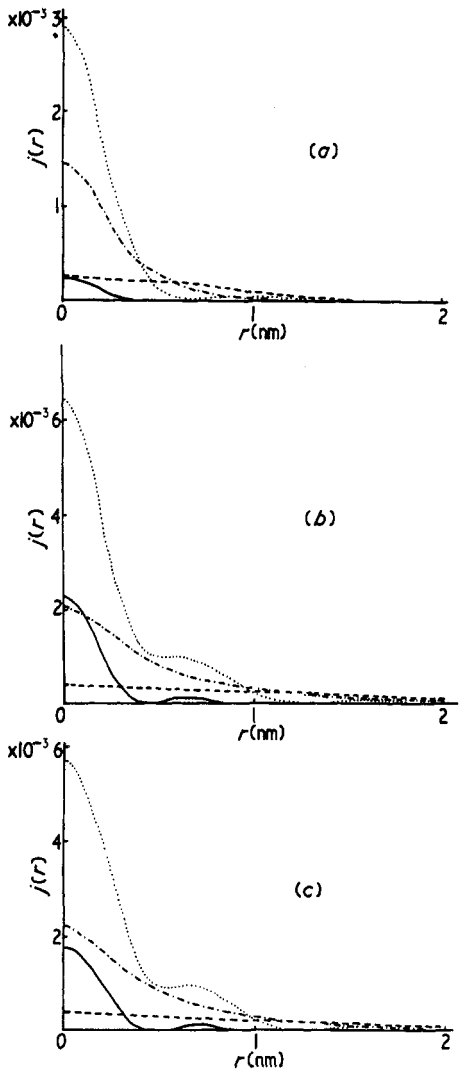

Figure 11. A comparison of the elastic dark-field image (full curve) with the inelastic image for $t = 10$ nm obtained in the absence of chromatic aberration ($C_c = 0$, dotted curve) for the optimum elastic defocus Δf_E. The inelastic images ($C_c = 2$ mm) for Δf_E (broken curve) and the optimum inelastic defocus Δf_I (chain curve) are also shown. (*a*) $\alpha = 0{\cdot}005$ rad, $\Delta f_E = 0$; (*b*) $\alpha = 0{\cdot}01$ rad, $\Delta f_E = -100$ nm; (*c*) $\alpha = 0{\cdot}015$ rad, $\Delta f_E = -100$ nm and in all cases $\Delta f_I = -500$ nm. $C_s = 2$ mm, $E_0 = 100$ keV.

Although the ratio of the scattering within the objective aperture, h_I/h_E, is significantly greater than unity, R is of the order of 1. If we allow for the fact that we have assumed inelastic scattering to be a localized phenomenon, we see that delocalization will further reduce the inelastic image intensity $j_i(0)$. Thus in dark-field conditions using a conventional electron microscope with an objective aperture $\alpha \geqslant 0{\cdot}01$ rad, the optimum image contrast is obtained with a defocus Δf_E with the inelastic component contributing only as a slowly varying background. At the optimum inelastic defocus $\Delta f_I \simeq -500$ nm, the elastic image exhibits a resolution vastly inferior to the inelastic image, but practically

Table 1. A comparison of the image resolution and image intensity for inelastic scattering and elastic scattering in dark-field microscopy. The radial halfwidth $r_{1/2}$ nm is calculated for the optimum elastic defocus Δf_E nm and the optimum inelastic defocus Δf_i nm. The ratio of the inelastic to elastic image intensity at $r_i = 0$ is R and the ratio of the inelastic to elastic scattering within the objective aperture α rad is h_i/h_E. Film thickness $t = 10$ nm, $E_0 = 100$ keV, $C_s = 2$ mm

	Elastic image Δf_E	Inelastic image Δf_E, $C_c = 2$ mm		Inelastic image Δf_i, $C_c = 2$ mm		Inelastic image Δf_E, $C_c = 0$		
α(rad)	$r_{1/2}$(nm)	$r_{1/2}$	R	$r_{1/2}$	R	$r_{1/2}$	R	h_i/h_E
0·005	0·39	1·78	1·0	0·50	5·7	0·48	11·6	17
0·01	0·20	1·29	0·2	0·39	0·9	0·24	2·8	6
0·015	0·22	1·28	0·2	0·38	1·2	0·26	3·3	4

it is unlikely that the microscopist will choose this large defocus value. If a smaller objective aperture $\alpha \simeq 0{\cdot}005$ rad is used, then the decision on the optimum defocus is not clear. In the case of the scanning microscope, the optimum defocus value is nearly the same for both elastic and inelastic images.

In practice dark-field conditions in the conventional microscope may be achieved either by tilting the incident electron beam or by using a centre stop in the condenser or objective aperture (Dupouy 1967, Dupouy *et al* 1969); in either case not only is the unscattered component removed but also a substantial fraction of the small-angle inelastic scattering. Assuming a centre stop corresponding to a semi-angle $\alpha_{min} = 0{\cdot}001$ rad, we see from figure 12 that the inelastic image intensity is reduced by up to a factor of 2 for the smallest aperture. Thus the elastic dark-field intensity $j_i(0)$, which is only marginally affected by a centre stop, exceeds the inelastic image intensity ($\Delta f = -500$ nm) for $\alpha = 0{\cdot}01$ and $0{\cdot}015$ rad by a factor of about 1·2.

6. Comparison of the inelastic image with the bright-field elastic image

In bright-field microscopy the unscattered wave (intensity represented by β^2, allowing for the attenuation of the incident beam of unit intensity by elastic and inelastic scattering) combines with the elastic wave $\exp(i\pi/2)|\Psi_E(\boldsymbol{\theta})|$. In the approximation that $\beta^2 \gg h_E(\alpha)$ ($\beta^2 = 0{\cdot}81$, $h_E \simeq 0{\cdot}02$ for $t = 10$ nm), the elastic bright-field image intensity is (eg Misell 1971a)

$$j_i(\boldsymbol{r}_i) = \beta^2 + \frac{2\beta K_0}{2\pi} \int |\Psi_E(\boldsymbol{\theta})| \sin(K_0\chi(\boldsymbol{\theta}))D(\boldsymbol{\theta}) \exp(-iK_0\boldsymbol{\theta} \cdot \boldsymbol{r}_i)\, d\boldsymbol{\theta}. \tag{7}$$

and $j_i - \beta^2$ (the background intensity) integrated over $\boldsymbol{r}_i$ is equal to $h_E(\alpha)$. Figure 13 shows the bright-field elastic image (full curve) corresponding to a defocus Δf_E; the background level β^2 has been subtracted. The three inelastic images corresponding to Δf_E (broken curve), Δf_i (chain curve) both for $C_c = 2$ mm, and Δf_E (dotted curve) with $C_c = 0$ are shown. The large factor between the elastic image intensity and the inelastic image intensity at $r_i = 0$ is evident even for $\alpha = 0{\cdot}005$ rad. Table 2 shows the comparison of the radial halfwidths of the elastic and inelastic image profiles and presents values for the ratio R. Thus in the conventional electron microscope the bright-field elastic image would appear to reduce the inelastic role to that of an unstructured background in the

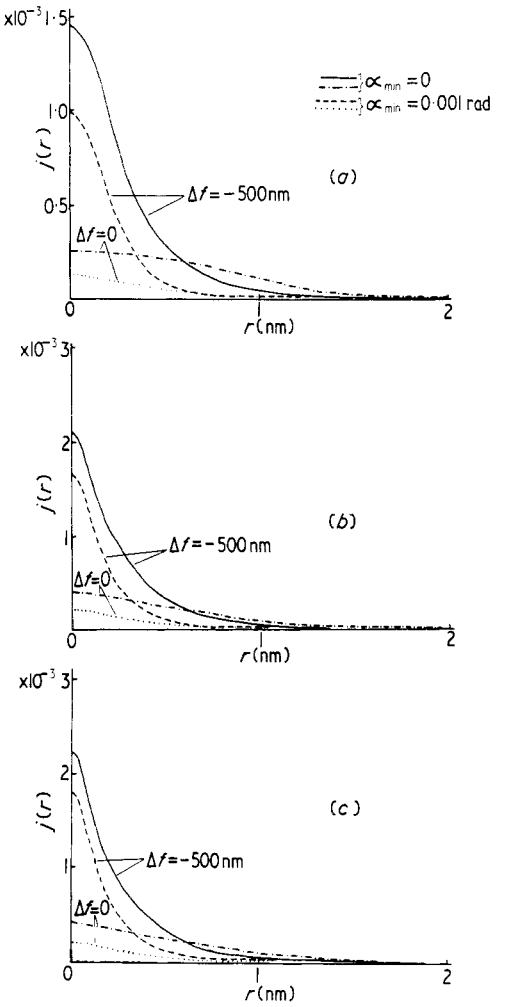

Figure 12. The effect of a centre stop (either in the condenser or objective aperture), semi-angle α_{min} rad, on the inelastic image intensity $j(r)$ for $t = 10$ nm and for defocus values of $\Delta f = 0, -500$ nm. (*a*) $\alpha = 0{\cdot}005$ rad, (*b*) $\alpha = 0{\cdot}01$ rad, (*c*) $\alpha = 0{\cdot}015$ rad. $C_c = C_s = 2$ mm, $E_0 = 100$ keV.

image. However, unlike the elastic dark-field image, the bright-field image does not converge rapidly to zero but oscillates about β^2 to radial values up to 2–3 nm. At defocus values $\Delta f_1 \simeq -500$ nm, the elastic bright-field image is inferior to the inelastic image.

In the case of thicker specimens ($t \simeq 50$ nm) the h_I/h_E ratio increases with t and β^2 is reduced to 0·35, and the elastic image contrast is reduced by a factor of about 4–10.

7. Conclusions

We have attempted to evaluate quantitatively the effect of chromatic aberration on the inelastic image obtained in the conventional electron microscope ($E_0 = 100$ keV),

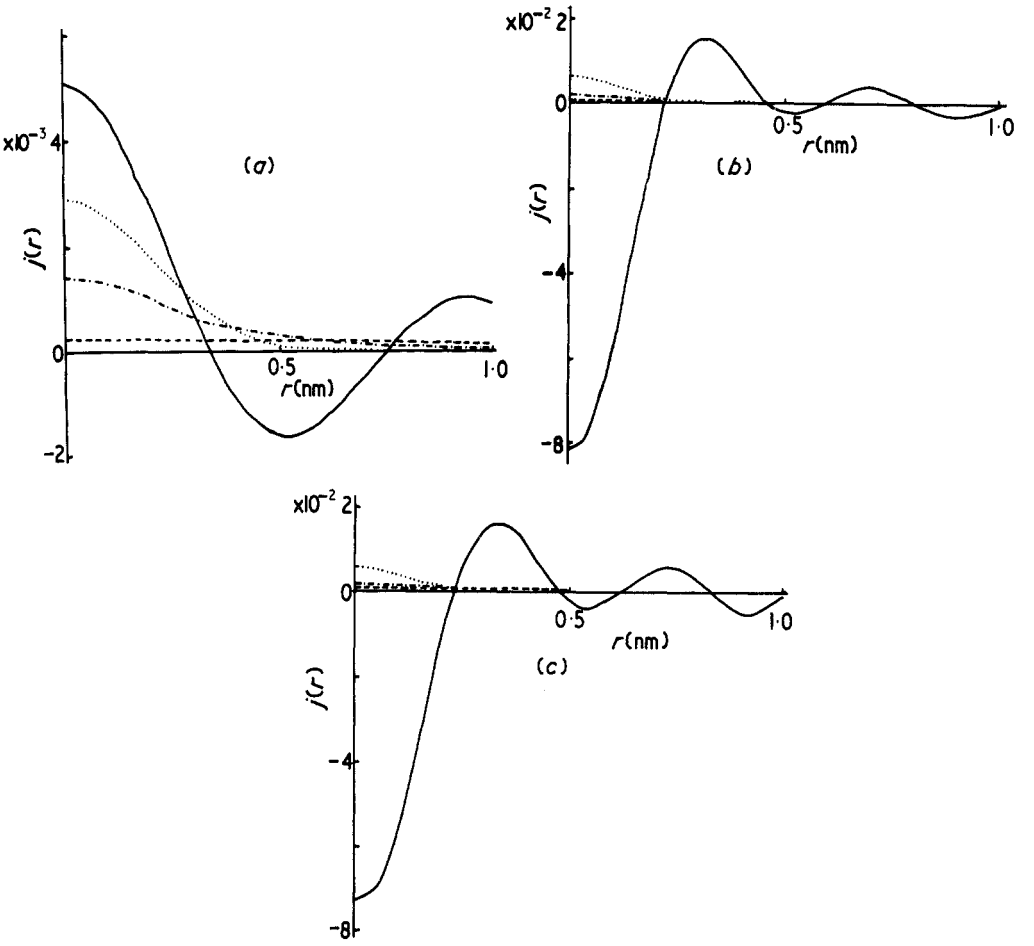

Figure 13. A comparison of the elastic bright-field image (full curve) with the inelastic image for $t = 10$ nm obtained in the absence of chromatic aberration ($C_c = 0$, dotted curve) for the optimum elastic defocus Δf_E. The inelastic images ($C_c = 2$ mm) for Δf_E (broken curve) and the optimum inelastic defocus Δf_I (chain curve) are also shown. (*a*) $\alpha = 0{\cdot}005$ rad, (*b*) $\alpha = 0{\cdot}01$ rad, (*c*) $\alpha = 0{\cdot}015$ rad. The background intensity (0·81) has been subtracted from the bright-field elastic image. $C_s = 2$ mm, $E_0 = 100$ keV.

Table 2. A comparison of the image resolution and image intensity for inelastic scattering and elastic scattering in bright-field microscopy. The radial halfwidth $r_{1/2}$ nm is calculated for the optimum elastic defocus Δf_E nm and the optimum inelastic defocus Δ_I nm. The ratio of the inelastic to elastic image intensity at $r_i = 0$ is R and the ratio of the inelastic to elastic scattering within the objective aperture α rad is h_I/h_E. $t = 10$ nm, $E_0 = 100$ keV, $C_s = 2$ mm

	Elastic image	Inelastic image		Inelastic image		Inelastic image		
	Δf_E	Δf_E, $C_c = 2$ mm		Δf_I, $C_c = 2$ mm		Δf_E, $C_c = 0$		
α(rad)	$r_{1/2}$(nm)	$r_{1/2}$	R	$r_{1/2}$	R	$r_{1/2}$	R	h_I/h_E
0·005	0·42	1·78	0·05	0·50	0·3	0·48	0·6	17
0·01	0·26	1·29	0·01	0·39	0·03	0·24	0·08	6
0·015	0·28	1·28	0·01	0·38	0·03	0·26	0·08	4

particularly in relation to biological specimens. In focus inelastic images ($\Delta f \simeq 0$) have a resolution of about 1·8 nm which varies only slightly with the objective aperture size ($\alpha = 0{\cdot}005$–$0{\cdot}015$ rad) and specimen thickness ($t = 10$–100 nm), although there is a significant thickness effect for radial distances greater than 2 nm. The optimum defocus value corresponding to maximum image intensity at $r_i = 0$ is about -500 nm, which varies slightly with α and t. Spherical aberration has a small effect on the inelastic image resolution except for the larger objective aperture $\alpha = 0{\cdot}015$ rad. In the conventional electron microscope the chromatic coherence of the inelastic scattering is irrelevant because of the large chromatic defect which destroys this coherence. The scanning transmission microscope with an effective $C_c = 0$ is suited to an evaluation of the coherence of the inelastic scattering. The only published inelastic micrographs of unstained biological sections are recorded at a low resolution in the scanning transmission microscope (Stroud *et al* 1969).

The assumption of a localized inelastic interaction favours the formation of a high resolution inelastic image; for metallic specimens delocalization, due to free electron effects, means that chromatic aberration is a secondary effect. If the delocalization in biological specimens is much greater than 0·5 nm, then the inelastic image resolution is further lowered.

Of relevance to the experimentalist is the comparison of the elastic and inelastic images obtained in the conventional microscope. In the dark-field microscopy of a thin specimen ($t = 10$ nm) the elastic image intensity is comparable with the inelastic image intensity, even though the ratio of inelastic to elastic scattering is about 4–20 (depending on α). In the scanning microscope the inelastic image intensity is still significantly greater than the dark-field elastic image intensity. For thicker films ($t = 50$ nm), the inelastic image is clearly the dominant feature of the dark-field image. In bright-field microscopy the elastic image intensity at $r_i = 0$ exceeds the inelastic image intensity by a factor 20–100 at the optimum elastic defocus value, although the oscillatory behaviour of the elastic image is a negative feature of this image. However, in bright-field conditions we must consider the inelastic scattering contributing to the total image only as a relatively unstructured background.

These considerations made in relation to the role of inelastic scattering in image formation in the conventional microscope and its subordinate role to the elastic image apply to high resolution images of the order of 0·5 nm. If we consider electron microscope images recorded at a resolution 1–2 nm, then the inelastic component is most relevant, since the image resolution is comparable with or larger than the present estimates of the chromatic defect.

Acknowledgments

The authors are grateful to Professor R E Burge for discussion and to the University of London Computing Centre for the provision of excellent computing facilities.

References

Cosslett V E 1969 *Z. angew. Phys.* **27** 138–41
Crewe A V 1970 *Q. Rev. Biophys.* **3** 137–75
Doyle P A 1970 *Acta Crystallogr.* A **26** 133–9

—— 1971 *Acta Crystallogr.* A **27** 109–16
Dupouy G 1967 *J. Electron Microsc., Japan* **16** 5–16
Dupouy G *et al* 1969 *C.R. Acad. Sci., Paris* B **268** 1341–5
Howie A 1963 *Proc. R. Soc.* A **271** 268–87
Kanaya K 1956a *Bull. electrotech. Lab., Japan* **20** 610–24
—— 1956b *Bull. electrotech. Lab., Japan* **20** 801–15
—— 1957 *Bull. Electrotech. Lab., Japan* **21** 455–74
Kanaya K, Inoue Y and Ishikawa A 1954 *J. Electron Microsc., Japan* **2** 1–7
Misell D L 1971a *J. Phys.* A: *Gen. Phys.* **4** 782–97
—— 1971b *J. Phys.* A: *Gen. Phys.* **4** 798–812
Stroud A N *et al* 1969 *Science* **164** 830–2